Mycobacterium tuberculosis KatG(S315T) Catalase−Peroxidase Retains All Active Site Properties for Proper Catalytic Function†

Sofia M. Kapetanaki,§ Salem Chouchane,⊥ Shengwei Yu,⊥ Xiangbo Zhao,⊥ Richard S. Magliozzo,⊥ and Johannes P. M. Schelvis*,§

Department of Chemistry, New York University, Room 1001, 31 Washington Place, New York, New York 10003, and Department of Chemistry, Brooklyn College and the Graduate Center of the City University of New York, 2900 Bedford Avenue, Brooklyn, New York 11210-2889

Received September 3, 2004; Revised Manuscript Received October 22, 2004

ABSTRACT: *Mycobacterium tuberculosis* (*Mtb*) KatG is a catalase−peroxidase that is thought to activate the antituberculosis drug isoniazid (INH). The local environment of *Mtb* KatG and its most prevalent INH-resistant mutant, KatG(S315T), is investigated with the exogenous ligands CO and NO in the absence and presence of INH by using resonance Raman, FTIR, and transient absorption spectroscopy. The Fe−His stretching vibration is detected at 244 cm^{-1} in the ferrous forms of both the wild-type enzyme and KatG(S315T). The ferrous−CO complex of both enzymes exhibits ν(CO), ν(Fe−CO), and δ(Fe−C−O) vibrations at 1925, 525, and 586 cm^{-1}, respectively, indicating a positive electrostatic environment for the CO complex, which is probably weakly hydrogen-bonded to a distal residue. The CO geometry is nonlinear as indicated by the unusually high intensity of the Fe−C−O bending vibration. The $\nu(Fe^{III}-NO)$ and $\delta(Fe^{III}-N-O)$ vibrations are detected at 596 and 571 cm^{-1}, respectively, in the ferric forms of wild-type and mutant enzyme and are indicative of a nonlinear binding geometry in support of the CO data. Although the presence of INH does not affect the vibrational frequencies of the CO- and NO-bound forms of either enzyme, it seems to perturb slightly their Raman intensities. Our results suggest a minimal, if any, perturbation of the distal heme pocket in the S315T mutant. Instead, the S315T mutation seems to induce small changes in the KatG conformation/dynamics of the ligand access channel as indicated by CO rebinding kinetics in flash photolysis experiments. The implications of these findings for the catalytic mechanism and mechanism of INH resistance in KatG(S315T) are discussed.

In the past decade, tuberculosis has reemerged as one of the leading causes of death worldwide due to an infectious disease because of the appearance of multidrug-resistant strains of *Mycobacterium tuberculosis* and the increased frequency of tuberculosis among individuals infected with the human immunodeficiency virus (HIV) (*1*). Isoniazid (INH)[1] has been the cornerstone in tuberculosis chemotherapy for half a century ever since its introduction as a potent antituberculosis drug in 1952 (*2*). Even though its mechanism of action is not fully understood, INH is generally believed to be a prodrug that is activated by the heme-containing catalase−peroxidase KatG, encoded by the *katG* gene (*3*−*8*). It has been proposed that the activated form of INH inhibits fatty acid synthase 2, an enzyme complex involved in mycolic acid biosynthesis (*9*−*11*), leading to cell death. Immediately after the introduction of INH, resistance to this drug was developed, which was linked in the majority of cases to mutations of the *katG* gene encoding the catalase−peroxidase. The most frequently encountered mutation is the S315T substitution, which has been found in over 50% of resistant isolates (*12*).

M. tuberculosis catalase−peroxidase (KatG) is a bifunctional enzyme that exists as a homodimer of 80-kDa subunits, both of which contain one heme iron (*13*, *14*). Besides catalase−peroxidase activity, KatG possesses Mn^{2+}-dependent peroxidase, cytochrome P450-like oxygenase, and peroxynitritase activities (*3*, *8*, *13*−*17*). The crystal structure of *Mtb* KatG has recently been resolved (*18*), as well as those from *Haloarcula marismortui* and *Burkholderia pseudomallei* (*19*, *20*). Although the arrangement of the catalytic residues arginine, tryptophan, and histidine in the distal heme pocket and the triad aspartic acid, tryptophan, and histidine in the proximal heme pocket are similar to class I peroxidases as previously suggested by sequence alignment of catalase−peroxidases (*21*), the structures reveal a deeply buried heme cofactor similar to that in a typical catalase (*18*−*20*). The most striking feature, however, is the unusual covalent linkage among three residues in the distal heme pocket, Trp107, Tyr229, and Met255 in *Mtb* KatG. The crystal

† This work was supported by a New York University Whitehead Fellowship for Junior Faculty in Biomedical or Biological Sciences (J.P.M.S.), the Heiser Program of the New York Community Trust (S.M.K.), and the National Institutes of Health Grant Number AI-43582 (R.S.M.).

* To whom correspondence should be addressed: tel, (212) 998 3597; fax, (212) 260 7905; e-mail, hans.schelvis@nyu.edu.

§ New York University.

⊥ Brooklyn College and the Graduate Center of the City University of New York.

[1] Abbreviations: *Mtb*, *Mycobacterium tuberculosis*; WT, wild-type; 6c, six coordinate; 5c, five coordinate; LS, low-spin; HS, high spin; INH, isoniazid (isonicotinic acid hydrazide); CCP, cytochrome *c* peroxidases; HRP, horseradish peroxidase; NP, nitrophorin; HmCP, *Haloarcula marismortui* catalase−peroxidase; BpKatG, *Burkholderia pseudomallei* catalase−peroxidase; *Mtb* KatG, *Mycobacterium tuberculosis* catalase−peroxidase.

10.1021/bi048097f CCC: $30.25
Published on Web 12/04/2004

structure of *Mtb* KatG shows that Ser315 is situated along a proposed substrate access channel and hydrogen bonds to a heme propionate as we had suggested on the basis of resonance Raman experiments (*18*, *22*).

Several models have been proposed for the inhibition of INH activation by the S315T mutation. On the basis of KatG−CO studies, it has been suggested that KatG(S315T) cannot activate INH because of its inability to form sufficient amounts of hydrogen-bonded oxy-KatG (*23*). Furthermore, based on sequence alignment with CCP and on the crystal structure of HmCP KatG, it has been proposed that steric interactions induced by the bulkier threonine hinder INH access to the heme pocket (*19*, *24*), which is consistent with spectroscopic and calorimetric experiments from our groups (*22*, *25*), though it cannot be ruled out that INH has a different binding site in the mutant. The crystal structure of BpKatG suggests an INH binding site outside the heme pocket, and it was proposed that changes in the hydrogen bond of Ser315 to a heme propionate would change the binding mode of the INH hydrazine group (*20*).

The binding mode of INH to KatG has not yet been established. NMR relaxation data have suggested that the distance between the heme iron and INH amide nitrogen is approximately 4 Å for both WT KatG and its S315T mutant (*26*). INH binding either inside or sufficiently close to the distal heme pocket was also suggested by Lukat-Rodgers et al. (*23*), but a different potential INH binding site in close proximity to Ser315 was identified in the crystal structure of BpKatG (*20*). Computational and modeling studies have argued against such a binding site in the surface loop, and it was suggested that the INH binding site is located near the *δ-meso* heme edge (*18*, *27*). On the basis of spectroscopic data, we have proposed a binding mode of INH to KatG that resembles that of BHA to HRP-C (*22*).

In this work, we use resonance Raman (RR) and FTIR spectroscopy to investigate the KatG catalytic site with the small exogenous ligands carbon monoxide (CO) and nitric oxide (NO). The vibrations associated with these exogenous ligands are excellent probes of the distal heme pocket, because they are very sensitive to changes in their environment induced by steric hindrance, electrostatic interactions, and substrate binding (*29*, *30*). The information inferred from the RR and FTIR spectra of the CO and NO complexes provides insight into the molecular basis of the catalytic activity of KatG and potential perturbations that are induced in the INH-resistant S315T mutant that affect, for example, substrate binding and the structural requirements for the catalytic mechanism. These small exogenous ligands are also excellent to obtain a better understanding of the nature of the binding and chemistry of peroxide and its critical dependence on the amino acid structure of the heme pocket (*28*). We report the ν(Fe−CO), ν(CO), and δ(Fe−C−O) frequencies of the CO complexes of ferrous WT KatG and KatG(S315T) in the absence and presence of INH, as well as the ν(Fe−NO) and δ(Fe−N−O) frequencies of their ferric complexes with nitric oxide (NO). We have also studied the ferrous form of WT KatG, KatG(S315T), and their INH complexes. The imidazolate character of the proximal histidine ligand as suggested by the ν(Fe−His) frequency, in combination with the positive polarity of the distal environment support the "push−pull" mechanism for O−O bond cleavage (*31*, *32*). We have also determined the CO rebinding kinetics of WT KatG and KatG(S315T) by employing the flash photolysis technique to investigate the effect of the S315T mutation on the accessibility of the heme pocket. The implications of our findings for the KatG catalytic mechanism and the mechanism of resistance to INH are discussed.

MATERIALS AND METHODS

Materials. CO (99.5%) and NO (99%) gases were purchased from Matheson Tri-Gas. The ^{13}CO (99%) and ^{15}NO (98%) isotopes were purchased from Cambridge Isotope Laboratories. All other reagents were from Sigma-Aldrich.

Isolation and Purification of M. tuberculosis Catalase−Peroxidase. *Mtb* catalase−peroxidase was isolated and purified from an overexpression system in *Escherichia coli* strain UM262 (KatG minus) expressing the *M. tuberculosis katG* gene, a gift from Stewart Cole (Institute Pasteur, Paris). The bacteria were grown in the presence of the heme biosynthetic precursor δ-aminolevulinic acid. WT KatG and KatG(S315T) were purified according to published procedures (*33*, *34*). The purified enzyme was in 20 mM potassium phosphate buffer at pH 7.2. All the samples used in this study were 2 weeks old to avoid changes in heme spin-state distribution due to aging of the protein (*22*). For the pH studies, KatG samples were exchanged into 20 mM citrate buffer at pH 5 or 20 mM borate buffer at pH 10.

Sample Preparation. The samples for the UV−vis and resonance Raman experiments were prepared and contained in a spinning cell that was sealed with a rubber septum. Typically, 60 μL of sample was used for each experiment. Ferrous KatG was prepared by injection of dithionite in a degassed buffer solution into a spinning cell containing ferric KatG under N_2 atmosphere. The CO adduct of ferrous KatG was made by purging CO gas into the cell. Separate optical and stopped flow experiments were used to evaluate the dissociation constant (K_d) and the on rate (k_{on}) for NO binding to ferric KatG, from which the off-rate (k_{off}) of NO was estimated (data not shown); $K_d = 116$ μM, $k_{on} = 1.39 \times 10^6$ M^{-1} s^{-1}, and $k_{off} = 1.6 \times 10^2$ s^{-1}. NO gas was first bubbled through a saturated KOH solution. The NO and ^{15}NO samples were prepared by injecting 200 μL of NO and ^{15}NO gas, respectively, from a vial containing nitrogen and KOH solution into a spinning cell containing ferric KatG under N_2 atmosphere. The formation of each KatG−ligand complex was verified by UV−vis spectroscopy.

Electronic Absorption and Resonance Raman Spectroscopy. Electronic absorption spectra were recorded at room temperature with a UV−vis spectrophotometer (Lambda P40, Perkin-Elmer). The resonance Raman (RR) spectra were obtained using a single spectrograph (TriAx 550, JY/Horiba) and a N_2(l)-cooled CCD detector (Spectrum One, JY/Horiba) with a UV-enhanced 2048 × 512 pixels chip (EEV). The spectral resolution is 4 cm^{-1}, and peak positions are determined with an accuracy of 1 cm^{-1}. The samples were excited with 413.1 nm light from a Kr^+ laser (Coherent, I-302) and kept at 6 ± 2 °C during the experiments. Rayleigh scattering was blocked by a 413.1 nm holographic notch filter (Kaiser Optical). Sample concentration was 40 μM, and the incident laser power was 10 and 1 mW for the KatG−NO and KatG−CO complexes, respectively. KatG−INH and

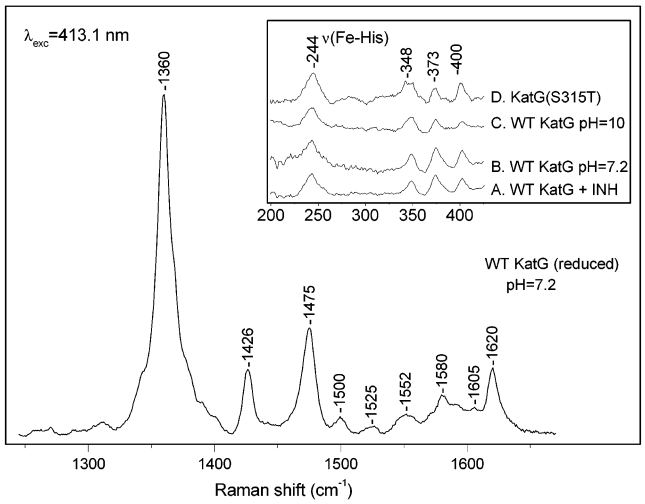

FIGURE 1: High-frequency resonance Raman spectrum of ferrous WT KatG at pH 7.2. The inset shows the 200−450 cm^{-1} region of ferrous wild-type KatG at pH 7.2 with (A) and without (B) INH and without INH at pH 10 (C) and of ferrous KatG(S315T) at pH 7.2 (D).

KatG(S315T)−INH complexes were made by addition of 70 and 500 equiv of INH, respectively. Background correction of RR spectra was done by subtraction of a smooth polynomial. Vibrations were labeled and assigned following the literature unless indicated differently (*35*−*37*). Toluene was used to calibrate the RR spectra.

Fourier Transform Infrared Spectroscopy. FTIR spectra were obtained from 500 μM samples with an AVATAR 360 FT-IR spectrometer equipped with a TGS detector. Anaerobic samples were loaded into a cell with CaF_2 windows and a 50 μm spacer. Each spectrum is averaged 512 times with 4 cm^{-1} resolution. Absorption spectra were taken before and after measurements to confirm sample stability.

CO Flash Photolysis Experiments. CO rebinding kinetics were recorded using a transient absorption system (7 ns response time) described previously (*38*). It consists of a Nd:YAG laser (Surelight SLII-10, Continuum) with 532 nm, 7 ns laser pulses at a 20 Hz repetition rate as an excitation source and a 75 W pulsed Xe lamp for probe light selected by a McPherson monochromator and detected by a Hamamatsu R928 photomultiplier. The output was digitized and recorded using a Tektronix TDS 620 oscilloscope. The CO samples were prepared in a 1 cm quartz cuvette. The laser light was focused with a quartz lens ($f = 1$ m) through a 3 mm × 9 mm aperture to obtain a uniform excitation intensity of ~62 mJ/cm^2 at the sample. Transient absorbance changes were probed at 445 nm through a 3 mm aperture perpendicular to the laser beam. The experiments were performed at 20 °C. The samples were stable under these conditions as judged from absorption spectra taken before and after the experiment and from successive flash photolyses of the same sample that yielded the same CO rebinding kinetics.

RESULTS

Ferrous KatG. Figure 1 shows the high-frequency RR spectrum of ferrous WT KatG obtained with Soret excitation. The oxidation state marker band ν_4 is observed at 1360 cm^{-1}, a frequency characteristic of ferrous hemes. The spin state marker ν_3 has one main contribution at 1475 cm^{-1}, indicating the presence of a pentacoordinated, high-spin (5c/HS) configuration (*28*) consistent with the absorption spectrum, which exhibits a Soret band at 439 nm and Q-bands at 559 and 590 nm (data not shown) characteristic of a 5c ferrous heme (*39*). The presence of a small amount of residual ferric, 5c/QS heme (*22*) cannot be excluded as indicated by weak ν_3 and ν_2 modes at 1500 and 1580 cm^{-1}, respectively. Since excitation at 413.1 nm favors enhancement of ferric 5c/QS heme ($\lambda_{max} \approx 406$ nm) over 5c/HS ferrous heme ($\lambda_{max} \approx 439$ nm), the total amount of residual ferric heme is expected to be very small. The vibrations at 1605 and 1620 cm^{-1} are attributed to the ν_{10} and a vinyl stretching mode (ν_{CC}) of the 5c/HS ferrous heme, respectively. Our results are nearly identical to those obtained with 441.6 nm excitation, which favors excitation of the 5c/HS ferrous heme, but we did not observe the 6c/LS ferrous heme, which was reported in a previous study (*40*). The vibrational frequencies resemble those of ferrous CCP at pH 7.2, which has ν_4, ν_3, ν_2, ν_{10}, and ν_{CC} at 1356, 1471, 1563, 1604, and 1618 cm^{-1}, respectively (*39*). Ferrous KatG(S315T) has the same visible and RR spectra as the WT enzyme (data not shown) with a predominant 5c/HS ferrous heme and a very small amount of ferric 5c/QS heme.

The inset of Figure 1 shows low-frequency RR spectra of ferrous KatG/INH complex (pH = 7.2, trace A), KatG (pH = 7.2, trace B), KatG (pH = 10, trace C), and KatG(S315T) (pH = 7.2, trace D). The prominent band at 244 cm^{-1} is assigned to ν(Fe−His), the stretching vibration of the Fe^{II}-proximal histidine moiety (*40*), which is a typical frequency for a proximal histidine with imidazolate character in peroxidases (*41*). We do not observe the second ν(Fe−His) at 228 cm^{-1} that was previously reported in KatG at pH 10 and in KatG(S315T), which argues against the proposed modification of the hydrogen-bonding environment of the proximal histidine ligand in ferrous KatG by the S315T mutation (*40*).

$KatG^{II}$−CO Complex. CO is an excellent probe of the distal heme pocket environment because it is very sensitive to electrostatic and steric interactions with nearby groups (*29*, *42*). It binds only to ferrous heme proteins, generally, in a nearly linear Fe−C−O geometry (*43*). The Fe−CO and C−O stretching frequencies are affected by the polarity near the Fe−CO moiety (*44*, *45*). In peroxidases, the relatively high ν(Fe−CO) frequency is attributed to an increase in Fe−CO bond order due to imidazolate character of the proximal histidine ligand and hydrogen bonding interactions of a distal pocket residue with CO (*44*).

Figure 2 shows the low-frequency RR spectra of the CO complexes of KatG in the presence of INH at pH 7.2 (trace A), at pH 7.2 with ^{12}CO (trace B) and ^{13}CO (trace C), and at pH 10 (trace D). In heme proteins, ν(Fe−CO) and the Fe−C−O bending vibration, δ(Fe−C−O), are expected at ca. 500 and 580 cm^{-1}, respectively (*29*). We detect two bands in the RR spectra at 525 and 586 cm^{-1} (traces A, B, and C) that shift to 519 and 569 cm^{-1}, respectively, in the ^{13}CO-bound adduct (trace D). The isotope difference spectrum is shown in inset I. We assign the 525 cm^{-1} band to ν(Fe−CO) and the 586 cm^{-1} band to δ(Fe−C−O) of the KatG−CO complex. The C−O stretching mode, ν(CO), is located at 1925 cm^{-1} (inset II), and the ^{13}CO isotope produces a 42 cm^{-1} downshift (data not shown). In deuterated buffer, a 1 cm^{-1} shift is observed for ν(CO) at pH 7.2 at the limit of our resolution, suggesting the existence of weak H-bond

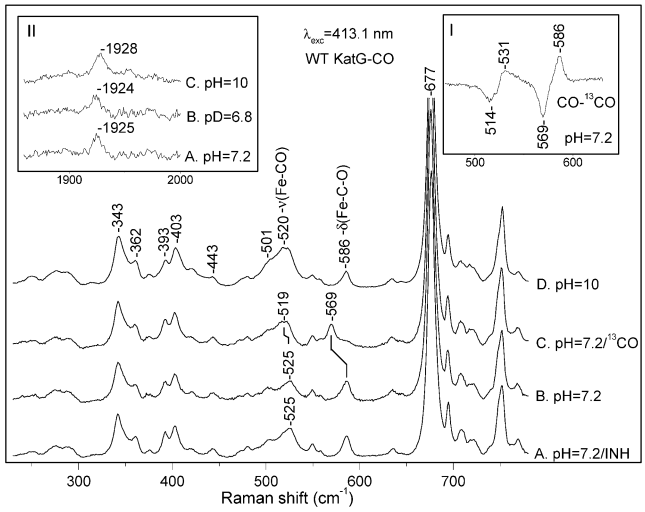

FIGURE 2: Low-frequency resonance Raman spectra of ferrous WT KatG−CO complex at pH 7.2 in the presence (A) and absence (B) of INH, at pH=7.2 with ^{13}CO (C), and at pH 10 (D). Inset I shows the difference spectrum of ferrous WT KatG−CO minus KatG-^{13}CO at pH 7.2. Inset II shows the resonance Raman spectra of ferrous WT KatG−CO in the 1850−2000 cm^{-1} region at pH 7.2 (A), at pD 6.8 (B), and at pH 10 (C).

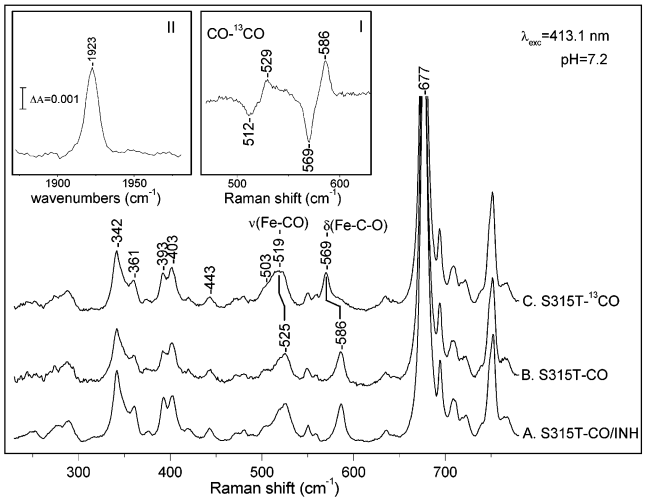

FIGURE 3: Low-frequency resonance Raman spectra of KatG(S315T)−CO at pH 7.2 in the presence of INH (A), without INH (B), and INH-free with ^{13}CO (C). Inset I shows the difference spectrum of KatG(S315T)−CO minus KatG(S315T)−^{13}CO at pH 7.2. Inset II shows the FTIR spectrum of KatG(S315T)−CO in D_2O in the 1850−2000 cm^{-1} region.

between CO and a distal residue. Addition of INH to KatG (70 equiv) at pH 7.2 (trace B) does not affect the vibrational frequencies of its CO complex, but it affects the intensities of ν(Fe−CO) and δ(Fe−C−O) slightly. In contrast, a 5 cm^{-1} downshift of ν(Fe−CO) is observed for KatG−CO at pH 10 (trace E), which is accompanied by a decrease in the intensity of δ(Fe−C−O) and a 3 cm^{-1} upshift of ν(C−O) (Figure 2, inset II, trace D), but ν(C−O) did not shift in deuterated buffer at this pH (data not shown).

The RR spectra of ferrous CO-bound KatG(S315T) in the absence and presence of INH show ν(Fe−CO) and δ(Fe−C−O) at 525 and 586 cm^{-1}, respectively, which shift to 519 and 569 cm^{-1}, respectively, in the ^{13}CO adduct (Figure 3) similar to WT KatG. The isotope difference spectrum is shown in inset I of Figure 3. In KatG(S315T)−CO, ν(CO) is observed at 1925 cm^{-1} in the Raman spectrum (data not shown) and at 1923 cm^{-1} in the FTIR spectrum (Figure 3, inset II). The small frequency shift is probably due to deuteration of a H-bond to a distal residue in the deuterated buffer for the FTIR experiment.

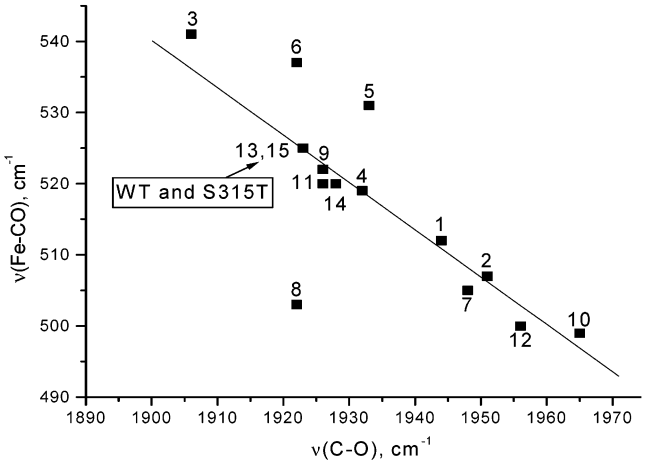

FIGURE 4: Correlation line of ν(Fe−CO) vs ν(C−O) for various peroxidases and KatG: KatG at pH 7.2 [13], KatG at pH 10 [14], and KatG(S315T) at pH 7.2 [15]. All entries are tabulated in the Supporting Information.

Extensive studies of CO complexes of heme proteins have shown that ν(Fe−CO) and ν(C−O) follow an inverse linear correlation due to π-electron back-donation from the d_π(d_{xz}, d_{yz}) orbitals of Fe^{II} to the empty π^* orbitals of CO (*29*). Placement along the ν(Fe−CO) vs ν(CO) correlation line reflects modulation of the back-bonding by polar groups in the distal heme pocket. Figure 4 shows a ν(Fe−CO) vs ν(CO) correlation that compares KatG to peroxidases. The data fall on a correlation line that is characteristic for hemoproteins with a proximal histidine ligand. Points high on the line, with ν(Fe−CO) > 520 cm^{-1} and ν(C−O) < 1935 cm^{-1}, are believed to reflect distal H-bond interactions to CO and a positively charged environment (*46*), indicating that such an environment is present in both WT and S315T KatG.

KatG^{III}−NO Complex. The NO complex of ferric KatG has an absorption spectrum with a Soret band at 421 nm and Q-bands at 535 and 570 nm (Figure 5, inset I), similar to HRP^{III}−NO (*47*). Figure 5 shows the high-frequency RR spectra of the ferric−NO complexes of KatG and KatG(S315T) and their INH bound forms at pH 7.2. The ν_4, ν_3, and ν_{10} bands appear at 1378, 1513, and 1644 cm^{-1}, respectively, and are indicative of 6c-ferric−nitrosyl complexes (*28*, *48*). Neither the S315T mutation nor addition of INH cause any changes in the vibrational frequencies. Inspection of the 1800−2000 cm^{-1} region did not reveal the ν(NO) vibration in agreement with previous observations in other histidine-containing hemoproteins excited in the Soret region, presumably due to little orbital conjugation between NO and the heme (*49*).

The S315T mutation, addition of INH, or both do not induce any changes in the frequencies of the low-frequency vibrations either (Figure 5). Only minor changes in the relative intensities of the 395 and 402 cm^{-1} vibrations and in the 270 cm^{-1} band shape occur in the S315T mutant. Isotope-sensitive bands are observed at 596 and 571 cm^{-1} for KatG−NO with corresponding bands at 589 and 561 cm^{-1} in the KatG−^{15}NO. The difference spectrum (^{14}NO −

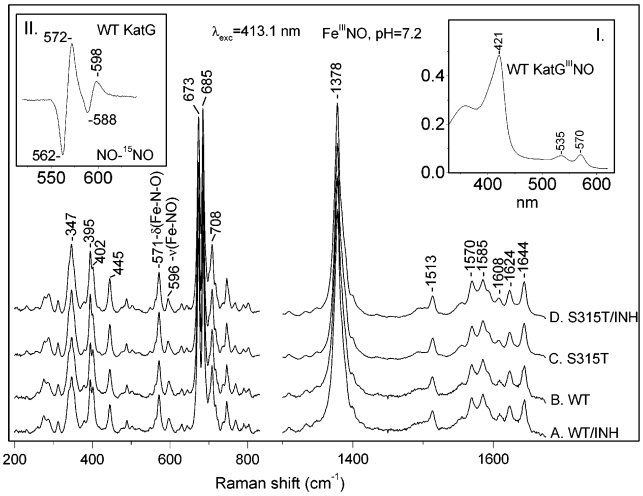

FIGURE 5: High- and low-frequency resonance Raman spectra of ferric KatG−NO at pH 7.2: (A) WT KatG−NO in the presence of INH; (B) WT KatG−NO; (C) KatG(S315T)−NO; (D) KatG(S315T)−NO in the presence of INH. Inset I shows the UV−vis spectrum of ferric WT KatG−NO at pH 7.2. Inset II shows the difference spectrum of ferric WT KatG−NO minus KatG−^{15}NO at pH 7.2.

Table 1: Frequencies (cm^{-1}) of the Fe−NO Modes in Selected Ferric Nitrosyl Heme Proteins

	ν(Fe−NO)	δ(Fe−N−O)	ν(N−O)	refs
Mb	595	573	1922	48, 79
HbA	594		1925	48, 80
HRP	604	574	1903	48
NP	591	578	1904	70, 81
Nor	594		1904	82
KatG	596	571		this work

^{15}NO) of the KatG−NO complex is shown in inset II of Figure 5. Based on the assignments for the Mb−NO complex (*48*), we assign the 596 and 571 cm^{-1} bands of KatG−NO to ν(Fe−NO) and δ(Fe−N−O), respectively. The ν(Fe−NO) frequency at 596 cm^{-1} is characteristic of a ferric 6c/LS NO complex, indicating a typical Fe^{III}−NO bond strength, and is 1 cm^{-1} higher in frequency than in ferric Mb−NO, while the δ(Fe−N−O) frequency at 571 cm^{-1} is lower by 2 cm^{-1} (see Table 1). Even though we observed three heme species in the ferric resting form of KatG (*22*), we detect only a single NO binding conformation to the heme, in agreement with the CO data.

The heme oxidation, coordination, and spin state markers of the ferric KatG−NO complex are not sensitive to pH as shown in Figure 6. The ν(Fe−NO) and δ(Fe−N−O) frequencies are also independent of pH and are observed at 596 and 571 cm^{-1}, respectively, with similar intensities.

CO Rebinding Kinetics. We measured the CO rebinding rates for both KatG and KatG(S315T) following flash photolysis at pH 7.2 and 1 mM CO. Figure 7 shows the transient absorption traces detected at 445 nm, at which wavelength the decay of photolyzed KatG−CO and KatG(S315T)−CO can be monitored to determine the CO rebinding rate. Best fits were obtained with a biexponential decay function, and the pseudo-first-order rates are summarized in Table 2. Recombination of CO has a fast phase with a relative amplitude of 13% ± 3% for KatG and of 14% ± 1% for KatG(S315T) with recombination rates of (5 ± 3) × 10^3 and (6.2 ± 1.8) × 10^3 s^{-1}, respectively. The slow phase

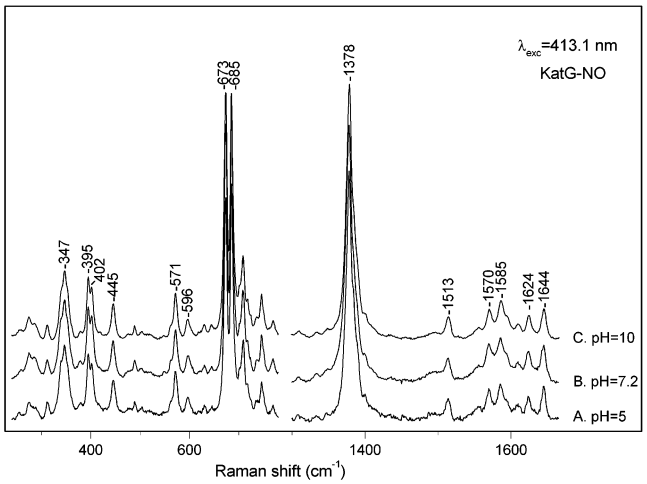

FIGURE 6: High- and low-frequency resonance Raman spectra of ferric KatG−NO complex at pH 5 (A), pH 7.2 (B), and pH 10 (C).

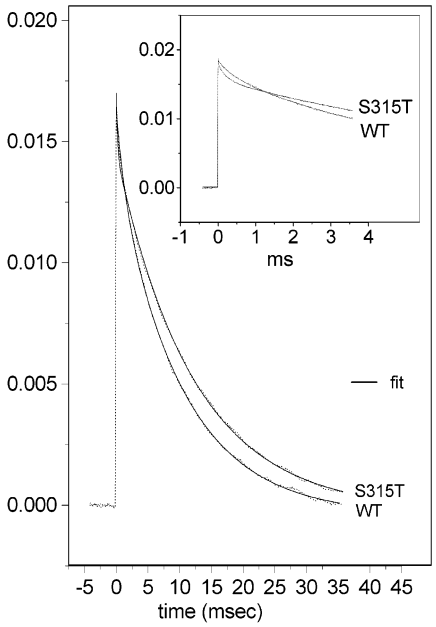

FIGURE 7: CO rebinding to KatG and KatG(S315T) following flash photolysis. Transient absorption traces at 445 nm of WT KatG (dotted line) and KatG(S315T) (dotted line). Biexponential fits to the data are shown with a straight line. The inset shows the fast rebinding phase.

Table 2: CO Rebinding Rates (k_1,k_2) and Normalized Amplitudes (A_1,A_2) for KatG and KatG(S315T)

	k_1 (10^3 s^{-1})	A_1	k_2 (s^{-1})	A_2
KatG	5 ± 3	0.13 ± 0.03	108 ± 11	0.87 ± 0.03
KatG(S315T)	6.2 ± 1.8	0.14 ± 0.01	84 ± 7	0.86 ± 0.01

dominates the recombination process accounting for 87% ± 3% in KatG and 86% ± 1% in KatG(S315T) with rates of 108 ± 11 and 84 ± 7 s^{-1}, respectively. The recombination rates in both KatG and KatG(S315T) are much faster compared to CCP (k_1 = 0.4 × 10^3, k_2 = 5 s^{-1}) (*50*) and HRP (k_1 = 0.004 × 10^3 s^{-1}) (*51*). However, the R38L HRP mutant has recombination kinetics (k_1 = 5 × 10^3, k_2 = 200 s^{-1}) that compare well to both KatG and KatG(S315T) (*51*).

DISCUSSION

We have obtained RR and FTIR spectra for the reduced, ferrous CO-bound, and ferric NO-bound forms of KatG and

KatG(S315T), which give new insight into the heme environment of *Mtb* KatG and ligand binding in general. Our data also provide a test for three models concerning the mode of antibiotic resistance in KatG(S315T) (*19*, *20*, *23*).

Proximal Heme Pocket. The low-frequency RR spectra of both KatG and KatG(S315T) reveal a band at 244 cm^{-1}, which has been assigned to the stretching vibration, ν(Fe−His), of the bond between the heme iron and the imidazole side chain of the proximal His270 (40). Its high frequency is comparable to that in peroxidases and is characteristic of the imidazolate character of the proximal histidine ligand, which is probably due to a hydrogen bond between the imidazole Nδ hydrogen and the Asp381, resulting in increased electron donation of Nϵ and an elevated ν(Fe−Nϵ(His)) frequency (*48*). The distance between proximal His270 and Asp381 is about 2.65 Å in *Mtb* KatG (pdb 1SJ2, *18*), very close to that in CCP (pdb 1CCP, 2.90 Å) and HRP-C (pdb 1ATJ, 2.74 Å) in which ν(Fe−His) is observed at 246−249 (*52*−*55*) and 244 cm^{-1} (*56*), respectively, supporting the presence of a polar hydrogen bond between His270 and the carboxylate group of Asp381 in *Mtb* KatG. In contrast to a previous study, we did not observe a second ν(Fe−His) at lower frequency, and our results argue against their proposal that the S315T mutation affects the H-bonding environment of the proximal histidine ligand in ferrous KatG (*40*). The high ν(Fe−His) frequency observed in both KatG and KatG(S315T) indicates strong proximal ligation, which makes the proximal histidine ligand a good electron donor, resulting in increased electron density at the heme iron, which helps to stabilize higher oxidation states of the heme iron and facilitates peroxidase activity, even in the S315T mutant. The stronger Fe−His270 bond further weakens the Fe^{IV}═O bond and, presumably, increases the chemical activity of compound I, which is formed after treatment of KatG with different peroxides (*33*) and KatG(S315T) with peroxyacetic acid (*25*). In conclusion, the S315T mutation seems to affect neither the proximal histidine ligation nor the chemical activity of compound I, and we do not believe that inhibition of INH activation in the S315T mutant is due to modification of hydrogen bonding to the proximal histidine ligand.

Distal Heme Pocket. The crystal structure of *Mtb* KatG (*18*) shows that it contains the conserved arginine, tryptophan, and histidine triad in the distal heme pocket similar to class I peroxidases. Distal tryptophan mutants of catalase−peroxidases are devoid of catalatic activity (*57*), while the distal histidine and arginine residues have been shown to play a significant role in peroxide activation in peroxidases (*31*).

Polarity. In both WT and S315T KatG, we find evidence for only one heme−CO conformer with ν(Fe−CO) = 525 cm^{-1}, δ(Fe−C−O) = 586 cm^{-1}, and ν(CO) = 1925 cm^{-1}. The position of ν(Fe−CO) and ν(CO) in the correlation plot (Figure 4) indicates a positively charged distal heme pocket, H-bonding to CO, or both. The latter is supported by small changes in ν(CO) upon H/D exchange and in ν(Fe−CO) and ν(CO) and the absence of an H/D effect at pH 10, presumably, due to deprotonation of the H-bond donor.

At neutral pH, HRP-C−CO has two conformers. In one complex, CO has been proposed to accept a hydrogen bond from distal Arg38 with ν(Fe−CO) at 519 cm^{-1} and ν(CO) at 1934 cm^{-1}. In the other, CO mainly interacts with distal His42 and displays ν(Fe−CO) at 541 cm^{-1} and ν(CO) at 1905 cm^{-1} (*58*, *59*). In CCP−CO, only one conformer is present, and CO is tilted 12° and H-bonded to a water molecule, which is H-bonded to Arg38 (60). However, the H42L−CO complex in both HRP-C and CCP has ν(Fe−CO) at 525 and 522 cm^{-1}, respectively, with ν(CO) at 1924 and 1928 cm^{-1}, respectively (*46*, *60*). In these complexes, CO has been proposed to interact with Arg38 by default. Although these frequencies are similar to those observed in KatG and KatG(S315T), we do not favor a stabilization mechanism that involves only the distal Arg104 in *Mtb*. Our results indicate that a hydrogen bonding residue is deprotonated at pH 10, which suggests involvement of distal His108 because arginine is expected to have a pK_a around 12. Furthermore, the position of KatG in the correlation plot is lower than HRP, indicating that CO experiences a less positively charged or hydrogen-bonding distal environment or both in *Mtb* KatG than in HRP. In support of this conclusion, the distance between the heme iron and the nitrogens of the distal arginine side chain is larger in *Mtb* KatG ($Fe-N_{arg} \geq 6.27$ Å, pdb 1SJ2, *18*) than in HRP ($Fe-N_{Arg} \geq 4.61$ Å, pdb 1ATJ, *61*).

Steric Factors. The inherent geometry of the Fe−XO (X = C, N) fragment of diatomic ligand adducts of metalloporphyrins or heme proteins depends on the total number of electrons in metal d_π and ligand π^* orbitals (*29*). In Fe^{II}−CO and Fe^{III}−NO complexes, a total of six electrons favors a linear geometry. If there is no distortion of the heme−CO geometry or asymmetry in the electrostatic potential of the surrounding protein, the bending mode is not present or very weak in the RR spectrum (*44*).

In the KatG−CO and KatG(S315T)−CO, the intensity of δ(Fe−C−O) is unusually high. Studies of heme model compounds have revealed that the intensity of δ(Fe−C−O) relative to ν(Fe−CO) is proportional to sterically induced tilting of CO away from the normal of the heme plane (*62*). Comparison of the ratio $I_{bend}/I_{stretch}$ for KatG at pH 7.2 and pH 10 and KatG(S315T) at pH 7.2 suggests that both KatG ($I_{bend}/I_{stretch}$ = 0.92) and KatG(S315T) ($I_{bend}/I_{stretch}$ = 0.93) have a significant tilted CO ligand, indicating that they share a similar geometry of the CO group at pH 7.2. A distorted heme−CO geometry for *Mtb* KatG is not surprising because its crystal structure (*18*) reveals a shorter distance between the heme iron and the Nϵ of distal histidine (5.6 Å) compared to CCP (5.8 Å) and HRP (6 Å). In lactoperoxidase, an $I_{bend}/I_{stretch}$ of ∼0.5 has been observed and has also been interpreted in terms of a tilted Fe−CO geometry (*63*). At pH 10, a decreased intensity of δ(Fe−C−O) in KatG suggests a less tilted CO moiety ($I_{bend}/I_{stretch}$ = 0.38), which is, presumably, due to less constraint and loss of hydrogen bonding caused by deprotonation of distal His108, in agreement with the change in ν(C−O) frequency. A pK_a of 8.7 has been proposed for the distal histidine in HRP-C−CO (*59*), and we expect an analogous pK_a for the *Mtb* KatG distal histidine. The $I_{bend}/I_{stretch}$ ratio in KatG−CO adducts at pH 7.2 is noticeably larger than that in sterically constrained model compounds ($I_{bend}/I_{stretch}$ < 0.5) (*62*), and steric factors alone cannot explain the intense δ(Fe−C−O) in KatG−CO. However, steric constraints have been suggested to enforce the polar interactions with distal residues and consequently a combination of steric and electrostatic effects can account for the strong activation of δ(Fe−C−O) (*64*, *65*).

The observation of an intense δ(Fe−N−O) supports the CO results. The Fe^{III}NO moiety is isoelectronic with Fe^{II}-CO and known to adopt a linear configuration normal to the heme plane (*66*). No δ(Fe−N−O) mode has been observed for unhindered NO complexes of ferric heme proteins (*67*, *68*). Therefore, detection of δ(Fe−N−O) in ferric KatG−NO suggests an off-axis influence that induces a slightly distorted Fe^{III}−N−O configuration (*67*, *69*), in agreement with our observation for $KatG^{II}$−CO. Normal coordinate analysis indicates that the difference between the stretching and bending frequencies becomes larger with decreasing Fe^{III}−N−O angle (*70*, *71*). This difference is larger in KatG−NO (25 cm^{-1}) than in Mb−NO (22 cm^{-1}) providing support for a slightly more distorted Fe^{III}−NO linkage in KatG (*60*). However, in HRP-C−NO, this difference (30 cm^{-1}) is larger than in KatG−NO suggesting a less distorted Fe^{III}−NO linkage in KatG than in HRP-C (*60*). However, little is known about the possible distortion of the NO adduct and the activation mechanism of δ(Fe−N−O). It has been shown that the δ(Fe−N−O) intensity depends weakly on tilting (*71*), and a tilted Fe−NO moiety in KatG can probably be excluded, favoring a bent configuration that is activated by distal polar interactions similar to the one that we propose for the isoelectronic ferrous−CO complex of KatG. The results for KatG(S315T) are identical to those of KatG, and we believe that CO and NO share the same bound configuration in both enzymes. Furthermore, since CO experiences a positively charged environment, O−O bond cleavage of bound peroxide can be facilitated by stabilizing the separating charge in both KatG and KatG(S315T).

Our data are quite different from those obtained by Lukat-Rodgers et al. (*23*, *40*), who observed two CO binding conformations in KatG−CO: one hydrogen-bonded to a distal residue (form I) and one non-hydrogen-bonded (form II). Since form II was predominant in KatG(S315T)−CO, they proposed that KatG(S315T) cannot activate INH because of its inability to form sufficient amounts of hydrogen-bonded oxy-KatG. The δ(Fe−C−O) in their complexes exhibits a weaker intensity ($I_{bend}/I_{stretch}$ ratios of 0.4 and 0.2 can be estimated from their data for KatG−CO and KatG(S315T)−CO, respectively). Since the position of their CO complexes in the correlation plot is similar to that of ours (Figure 4), we exclude significant differences in distal pocket polarity, and we attribute the more intense δ(Fe−C−O) in our results to a more constrained distal environment. They also observed a 6c/LS heme species in ferrous KatG, which was more prevalent in KatG(S315T), and they suggested decreased access of oxygen or superoxide to the heme iron in the mutant. Consequently, a lower yield of the oxy-intermediate was expected in KatG(S315T), which has previously been considered as one of the pathways for activation of INH (*14*, *72*, *73*), though new results indicate that INH is mainly activated by reacting with compound I (*25*, *33*). Our results do not support their model that KatG(S315T) lacks sufficient hydrogen-bonding to exogenous ligands (*23*), because we observe only the hydrogen-bonded conformer in the CO complex of both KatG and KatG(S315T) and no 6c/LS ferrous heme. We have observed differences between our and their results before, and we believe that they may be due to differences in the isolation/purification procedure and, perhaps, storage of the enzyme (*22*, *34*). Our analysis of ferrous KatG and KatG(S315T) and of the Fe^{II}−CO and Fe^{III}−NO complexes indicates that the heme pocket in both KatG and KatG(S315T) is very similar and supports a bent configuration of distal ligands and seems optimized for binding O_2 and H_2O_2 in their preferred nonlinear conformation (*43*, *44*).

Interaction of INH with the CO and NO Complexes. Previous studies have demonstrated that INH affects the coordination state of the heme iron in ferric KatG and KatG(S315T) (*23*, *22*, *33*, *74*). However, addition of INH to KatG or KatG(S315T) does not change the vibrational frequencies in their CO and NO adducts but affects their intensities slightly. $I_{bend}/I_{stretch}$ decreases from 0.92 to 0.68 in KatG−CO/INH and from 0.93 to 0.87 in KatG(S315T)−CO/INH. Since the frequencies do not change, we rule out that INH binding affects the polarity of the distal heme pocket. It is more likely that INH binding lowers the relative intensity of δ(Fe−C−O) by lowering the steric constraints. The fact that the change is smaller for KatG(S315T) than for KatG is in excellent agreement with the observed reduced affinity of INH for KatG(S315T) (*25*). NMR experiments have suggested that the distance between the heme iron and an INH amide nitrogen is about 4 Å in both KatG and KatG(S315T) (*26*). The latter result is somewhat surprising given the low affinity of INH for the mutant (*25*). We have proposed similarities between INH binding in KatG and the nearly parallel orientation of BHA with respect to the heme in HRP-C (*22*, *75*). Recent modeling and computational studies have proposed a similar binding site that is located near the *δ-meso* heme edge (*18*, *27*). However, based on the crystal structure of BpKatG a different binding site for INH has been suggested (*20*), which is more than 10 Å away from the heme compared to BHA in HRP-C, but in close proximity to Ser315. In the HRP−CO/BHA ternary complex, the Fe−CO conformation changes from a mixture of non-H-bonded and H-bonded forms to a single H-bonded form (*76*). A similar effect of INH binding on the KatG−CO complex has been reported (*23*). We did not observe this effect because our samples have only the H-bonded CO conformer in both the absence and the presence of INH. Although our present results are not in disagreement with our previous suggestion of an INH binding site inside the KatG heme pocket similar to that of BHA in HRP, we cannot rule out an INH binding site outside the heme pocket close to the S315 residue. In the latter case, INH binding would reduce constraints on CO in the heme pocket through allosteric interactions.

CO Rebinding Kinetics. Our results on the CO rebinding kinetics to KatG following flash photolysis provide insight into the accessibility of the KatG heme pocket. Although the S315T mutation affects the CO rebinding rate, the effect is small. Both KatG and KatG(S315T) display a fast rebinding phase with similar amplitudes and rebinding rates within experimental error. They also have similar amplitudes for the slow phase, but the rebinding rate is slightly faster in KatG than in KatG(S315T). The results suggest small differences in the heme pocket, the access channel between KatG and KatG(S315T), or both. Our RR studies of the CO and NO complexes of KatG and KatG(S315T) indicate no significant differences in their distal heme pockets and proximal ligation. Therefore, the small difference in CO rebinding to the two enzymes most likely arises from differences in access to the heme pocket. It has been proposed

that the threonine-methyl group in KatG(S315T) causes steric hindrance in the heme access channel (*19*, *24*). Although CO is small, the perturbation induced by the bulky methyl group can still affect its access to the heme. Other factors, like conformational changes of internal cavities caused by the mutation, may also be responsible for the observed difference in the CO rebinding kinetics. It has also been suggested that the highly oriented water molecules in the access channel in *E. coli* HPII catalase facilitate H_2O_2 entry into the heme pocket (*77*). Therefore, perturbation of the water molecules in the access channel in KatG(S315T) could potentially affect the accessibility of CO and molecules such as peroxides or INH to the heme pocket. The proposed loss of one hydrogen bond to the heme-7-propionate in the S315T mutant may induce reorientation of these water molecules (*22*).

The faster recombination kinetics of CO in *Mtb* KatG compared to CCP and HRP suggests that there may be significant differences in the access channels between the catalase−peroxidases and class I peroxidases. This is not a surprise if one takes into consideration the catalatic activity of catalase−peroxidases, which requires separate inlet and outlet channels to let the rapidly evolving oxygen escape without interfering with incoming substrate (*78*). The proposed heme access channel of a catalase−peroxidase is longer and more constricted compared to that of a peroxidase (*19*, *20*), which may hinder the escape and re-entry of CO into and from the solvent, opposite to our observations. Closer inspection of the crystal structures shows that the distal arginine in HRP is located closer to the heme iron than that in the three catalase−peroxidases (vide infra). Interference from the distal arginine may explain the slower CO rebinding kinetics in HRP compared to *Mtb* KatG. This proposal is supported by the comparable recombination kinetics of R38L HRP with respect to KatG and KatG(S315T) (*51*). Furthermore, the distal arginine does not seem to interfere with the proposed heme access channel in KatG (*19*). Consequently, the faster recombination rates in KatG compared to peroxidases may be attributed to the existence of more than one access channel, less crowding of the distal arginine over the heme iron, or both.

Conclusions. Our results provide an important test of several models that have been proposed for the inhibition mechanism of INH activation in KatG(S315T). We observed the same ν(Fe−His) properties in both KatG and KatG(S315T), and no differences were detected between the CO and NO complexes of the two enzymes. Therefore, we believe that neither modification of the hydrogen-bonding environment near the proximal histidine ligand nor lack of distal hydrogen bond formation to small exogenous ligands in KatG(S315T) results in inhibition of INH oxidation. In contrast, the strong Fe−His bond in both enzymes indicates an increased electron density in the heme iron, which can stabilize the higher oxidation states of the heme iron (compound I) and facilite the peroxidase and catalase activity, while the positive polarity in the distal pocket can stabilize the compound 0 and compound III intermediates. The observation of a single nonlinear binding geometry in $KatG^{II}$−CO and $KatG^{III}$−NO in both KatG and KatG(S315T) seems optimized for binding O_2 and H_2O_2 in their favored bent configuration. Our data suggest that the KatG S315T mutant retains all the structural requirements for proper catalytic function. Substitution of Ser315 with threonine affects the CO rebinding kinetics, which supports the proposal that the mutation confers resistance to INH by reducing accessibility to the KatG heme pocket by steric hindrance in the access channel. Since the actual binding site of INH in KatG and KatG(S315T) remains elusive, this model may only be relevant when INH binds inside the heme pocket, and modification of an INH binding site outside the heme pocket by the mutation cannot be ruled out.

ACKNOWLEDGMENT

We thank Dr. V. Shafirovich in the NYU DNA Chemistry and Photophysics Laboratory for his help with the CO flash photolysis experiments and the reviewers for their stimulating comments.

SUPPORTING INFORMATION AVAILABLE

Table with the frequencies (cm^{-1}) of the Fe−CO modes in selected heme proteins that are used for construction of Figure 4. This material is available free of charge via the Internet http://pubs.acs.org.

REFERENCES

1. World Health Organization (2002) *World Health Report*.
2. Fox, H. H. (1952) The chemical approach to the control of tuberculosis, *Science 116*, 129−134.
3. Johnsson, K., and Schultz, P. G. (1994) Mechanistic studies of the oxidation of isoniazid by the catalase-peroxidase from *Mycobacterium tuberculosis*, *J. Am. Chem. Soc. 116*, 7425−7426.
4. Quemard, A., Dessen, A., Sugantino, M., Jacobs, W. R., Jr., Sacchettini, J. C., and Blanchard, J. S. (1996) Binding of Catalase-Peroxidase-Activated Isoniazid to Wild-Type and Mutant *Mycobacterium tuberculosis* Enoyl-ACP Reductases, *J. Am. Chem. Soc. 118*, 1561−1562.
5. Basso, L. A., Zheng, R., and Blanchard, J. S. (1996) Kinetics of inactivation of WT and C243S mutant of *Mycobacterium tuberculosis* enoyl reductase by activated isoniazid, *J. Am. Chem. Soc. 118*, 11301−11302.
6. Johnson, K., King, D. S., and Schultz, P. G. (1995) Studies on the Mechanism of Action of Isoniazid and Ethionamide in the Chemotherapy of Tuberculosis, *J. Am. Chem. Soc. 117*, 5009−5010.
7. Basso, L. A., Zheng, R., Musser, J. M., Jacobs, W. R., Jr., and Blanchard, J. S. (1998) Mechanisms of isoniazid resistance in *Mycobacterium tuberculosis*: enzymic characterization of enoyl reductase mutants identified in isoniazid-resistant clinical isolates, *J. Infect. Dis. 178*, 769−775.
8. Wengenack, N. L., Jensen, M. P., Rusnak, F., and Stern, M. K. (1999) *Mycobacterium tuberculosis* KatG Is a Peroxynitritase, *Biochem. Biophys. Res. Commun. 256*, 485−487.
9. Banerjee, A., Dubnau, E., Quemard, A., Balasubramanian, V., Um, K. S., Wilson, T., Collins, D., deLisle, G., and Jacobs, W. R., Jr. (1994) inhA, a gene encoding a target for isoniazid and ethionamide in *Mycobacterium tuberculosis*, *Science 263*, 227−230.
10. Quemard, A., Sacchettini, J. C., Dessen, A., Vilcheze, C., Bittman, R., Jacobs, W. R., Jr., and Blanchard, J. S. (1995) Enzymatic characterization of the target for isoniazid in *Mycobacterium tuberculosis*, *Biochemistry 34*, 8235−8241.
11. Mdluli, K., Slayden, R. A., Zhu, Y., Ramaswamy, S., Pan, X., Mead, D. D., Musser, J. M., and Barry, C. E., III (1998) Inhibition of a *Mycobacterium tuberculosis* β-ketoacyl ACP synthase by isoniazid, *Science 280*, 1607−1610.
12. Slayden, R. A., and Barry, C. E., III (2000) The genetic and biochemistry of isoniazid resistance in *Mycobacterium tuberculosis*, *Microbes Infect. 2*, 659−669.
13. Johnsson, K., Froland, W. A., and Schultz, P. G. (1997) Overexpression, purification, and characterization of the catalase-

peroxidase KatG from *Mycobacterium tuberculosis*, *J. Biol. Chem. 272*, 2834−2840.
14. Magliozzo, R. S., and Marcinkeviciene, J. A. (1996) Evidence for isoniazid oxidation by oxyferrous Mycobacterial catalase-peroxidase, *J. Am. Chem. Soc. 118*, 11303−11304.
15. Marcinkeviciene, J. A., Magliozzo, R. S. and Blanchard, J. S. (1995) Purification and characterization of the *Mycobacterium smegmatis* catalase-peroxidase involved in isoniazid activation, *J. Biol. Chem. 270*, 22290−22295.
16. Magliozzo, R. S., and Marcinkeviciene, J. A. (1997) The role of Mn(II)-peroxidase activity of mycobacterial catalase-peroxidase in activation of the antibiotic isoniazid, *J. Biol. Chem. 272*, 8867−8870.
17. Wengenack, N. L., Uhl, J. R., St. Amand, A. L., Tomlinson, A. J., Benson, L. M., Naylor, S., Kline, B. C., Cockerill, F. R., and Rusnak, F. (1997) Recombinant *Mycobacterium tuberculosis* KatG(S315T) is a competent catalase-peroxidase with reduced activity toward isoniazid, *J. Infect. Dis. 176*, 722−727.
18. Bertrand, T., Eady, N. A. J., Jones, J. N., Nagy, J. M., Jamart-Grégoire, B., Raven, E. L., and Brown, K. A. (2004) Crystal structure of *Mycobacterium tuberculosis* catalase-peroxidase, *J. Biol. Chem. 279*, 38991−38999.
19. Yamada, Y., Fujiwara, T., Sato, T., Igarashi, N., and Tanaka, N. (2002) The 2.0 ANG. crystal structure of catalase-peroxidase from *Haloarcula marismortui*, *Nat. Struct. Biol. 9*, 691−695.
20. Carpena, X., Loprasert, S., Mongkolsuk, S., Switala, J., Loewen, P. C., and Fita, I. (2003) Catalase-peroxidase KatG of *Burkholderia pseudomallei* at 1.7.ANG. resolution. *J. Mol. Biol. 327*, 475−489.
21. Heym, B., Zhang, Y., Poulet, S., Young, D., and Cole, S. (1993) Characterization of the katG gene encoding a catalase-peroxidase required for the isoniazid susceptibility of *Mycobacterium tuberculosis*, *J. Bacteriol. 175* (13), 4255−4259.
22. Kapetanaki, S., Chouchane, S., Girotto, S., Yu, S., Magliozzo, R. S., and Schelvis, J. P. M. (2003) Conformational Differences in *Mycobacterium tuberculosis* Catalase-Peroxidase KatG and Its S315T Mutant Revealed by Resonance Raman Spectroscopy, *Biochemistry 42*, 3835−3845.
23. Lukat-Rodgers, G. S., Wengenack, N. L., Rusnak, F., and Rodgers, K. R. (2001) Carbon Monoxide Adducts of KatG and KatG-(S315T) as Probes of the Heme Site and Isoniazid Binding, *Biochemistry 40*, 7149−7157.
24. Saint-Joanis, B., Souchon, H., Wilming, M., Johnsson, K., Alzari, P. M., and Cole, S. T. (1999) Use of site-directed mutagenesis to probe the structure, function and isoniazid activation of the catalase/peroxidase, KatG, from *Mycobacterium tuberculosis*, *Biochem. J. 338*, 753−760.
25. Yu, S., Girotto, S., Lee, C., and Magliozzo, R. S. (2003) Reduced Affinity for Isoniazid in the S315T Mutant of *Mycobacterium tuberculosis* KatG Is a Key Factor in Antibiotic Resistance, *J. Biol. Chem. 278*, 14769−14775.
26. Todorović, S., Juranić, N., Macura, S., and Rusnak, F. (1999) Binding of 15N-Labeled Isoniazid to KatG and KatG(S315T): Use of Two-Spin [zz]-Order Relaxation Rate for 15N−Fe Distance Determination. *J. Am. Chem. Soc. 121*, 10962−10966.
27. Pierattelli, R., Banci, L., Eady, N. A. J., Bodigue, J., Jones, J. N., Moody, P. C. E., Raven, E. L., Jamart-Gregoire, B., and Brown, K. A. (2004) Enzyme-catalyzed mechanism of isoniazid activation in Class I and Class III peroxidases, *J. Biol. Chem. 279*, 39000−39009.
28. Spiro, T. G., and Li, X.-Y. (1988) Resonance Raman Spectroscopy of Metalloporphyrins, in *Biological Applications of Raman Spectroscopy* (Spiro, T. G., Ed.) Vol. 3, pp 1−37, Wiley, New York.
29. Yu, N.-T., and Kerr, E. A. (1988) Vibrational Modes of Coordinated CO, CN^-, O_2, and NO, in *Biological Applications of Raman Spectroscopy* (Spiro, T. G., Ed.) Vol. 3, pp 39−95, Wiley, New York.
30. Wang, J., Caughey, W. S., and Rousseau, D. L. (1996) Resonance Raman scattering: a probe of heme protein-bound nitric oxide, *Methods* in *Nitric Oxide Research* (Feelisch, M., and Stamler, J. S., Eds.) pp 427−454, Wiley, Chichester, U.K.
31. Poulos, T. L. (1988) Heme enzyme crystal structures, *Adv. Inorg. Biochem. 7*, 1−36.
32. Dawson, J. H. (1988) Probing structure−function relations in heme-containing oxygenases and peroxidases, *Science, 240*, 433−439.
33. Chouchane, S., Lippai, I., and Magliozzo, R. S. (2000) Catalase-Peroxidase (*Mycobacterium tuberculosis* KatG) Catalysis and Isoniazid Activation, *Biochemistry 39*, 9975−9983.
34. Chouchane, S., Girotto, S., Kapetanaki, S., Schelvis, J. P. M., Yu, S., and Magliozzo, R. S. (2003) Analysis of heme structural heterogeneity in *Mycobacterium tuberculosis* catalase-peroxidase (KatG), *J. Biol. Chem. 278*, 8154−8162.
35. Abe, M., Kitagawa, T., Kyogoku, Y. (1978) Resonance Raman spectra of octaethylporphyrinatonickel(II) and meso-deuterated and nitrogen-15 substituted derivatives. II. A normal coordinate analysis, *J. Chem. Phys. 69*, 4526−4534.
36. Choi, S., and Spiro, T. G. (1983) Out-of-plane deformation modes in the resonance Raman spectra of metalloporphyrins and heme proteins, *J. Am. Chem. Soc. 105*, 3683−3692.
37. Choi, S., Lee, J. J., Wei, Y. H., and Spiro, T. G. (1983) Resonance Raman and electronic spectra of heme a complexes and cytochrome oxidase, *J. Am. Chem. Soc. 105*, 3692−3707.
38. Shafirovich, V., Dourandin, A., Huang, W., Luneva, N. P., and Geacintov, N. E. (1999) Oxidation of Guanine at a Distance in Oligonucleotides Induced by Two-Photon Photoionization of 2-Aminopurine, *J. Phys. Chem. B 103*, 10924−10933.
39. Wang, J., Boldt, N. J., and Ondrias, M. R. (1992) Formation and photolability of low-spin ferrous cytochrome *c* peroxidase at alkaline pH, *Biochemistry 31*, 867−878.
40. Lukat-Rodgers, G. S., Wengenack, N. L., Rusnak, F., and Rodgers, K. R. (2000) Spectroscopic Comparison of the Heme Active Sites in WT KatG and Its S315T Mutant, *Biochemistry 39*, 9984−9993.
41. Kitagawa, T. in *Biological Applications of Raman Spectroscopy* (Spiro, T. G., Ed.) Vol. 3, p 97, Wiley, New York.
42. Kushkuley, B., and Stavrov, S. S. (1996) Theoretical study of the distal-side steric and electrostatic effects on the vibrational characteristics of the FeCO unit of the carbonylheme proteins and their models, *Biophys. J. 70*, 1214−1229.
43. Spiro, T. G., and Kozlowski, P. M. (2001) Is the CO adduct of myoglobin bent, and does it matter? *Acc. Chem. Res. 34*, 137−144.
44. Spiro, T. G., Zgierski, M. Z., and Kozlowski, P. M. (2001) Stereoelectronic factors in CO, NO and O_2 binding to heme from vibrational spectroscopy and DFT analysis, *Coord. Chem. Rev. 219*−*221*, 923−936.
45. Phillips, G. N., Jr., Teodoro, M. L., Li, T., Smith, B., and Olson, J. S. (1999) Bound CO is a molecular probe of electrostatic potential in the distal pocket of myoglobin, *J. Phys. Chem. B 103*, 8817−8829.
46. Smulevich, G., Mauro, M. J., Fishel, L. A., English, A. M., Kraut, J., and Spiro, T. G. (1988) Cytochrome *c* peroxidase mutant active site structures probed by resonance Raman and infrared signatures of the CO adducts, *Biochemistry 27*, 5486−5492.
47. Dawson, J. H., Kadkhodayan, S., Zhuang, C., and Sono, M. (1992) On the use of iron octa-alkylporphyrins as models for protoporphyrin IX-containing heme systems in studies employing magnetic circular dichroism spectroscopy, *J. Inorg. Biochem. 45*, 179−192.
48. Benko, B., and Yu, N.-T. (1983) Resonance Raman studies of nitric oxide binding to ferric and ferrous hemoproteins: Detection of iron(III)-nitric oxide stretching, iron(III)-nitrogen-oxygen bending, and iron(II)-nitrogen-oxygen bending vibrations, *Proc. Natl. Acad. Sci. U.S.A. 80*, 7042−7046.
49. Tomita, T., Haruta, N., Aki, M., Kitagawa, T., and Ikeda-Saito, M. (2001) UV Resonance Raman Detection of a Ligand Vibration on Ferric Nitrosyl Heme Proteins, *J. Am. Chem. Soc. 123*, 2666−2667.
50. English, A. M., McLendon, G., and Taylor, K. (1984) Kinetics of CO binding to cytochrome *c* peroxidase: pH and CO concentration effects, *J. Am. Chem. Soc. 106*, 6448−6449.
51. Meunier, B., Rodriguez-Lopez, J. N., Smith, A. T., Thorneley, R. N. F., and Rich. P. R. (1995) Laser photolysis behavior of ferrous horseradish peroxidase with carbon monoxide and cyanide: effects of mutations in the distal heme pocket, *Biochemistry 34*, 14687−14692.
52. Teraoka, J., and Kitagawa, T. (1981) Structural implication of the heme-linked ionization of horseradish peroxidase probed by the Fe-histidine stretching Raman line, *J. Biol. Chem. 256*, 3969−3977.
53. Hashimoto, S., Teraoka, J., Inubushi, T., Yonetani, T., and Kitagawa, T. (1986) Resonance Raman study on cytochrome *c* peroxidase and its intermediate. Presence of the iron(IV)═O bond in compound ES and heme-linked ionization, *J. Biol. Chem. 261*, 11110−11118.

54. Smulevich, G., Mauro, J. M., Fishel, L. A., English, A. M., Kraut, J., and Spiro, T. G. (1988) Heme pocket interactions in cytochrome *c* peroxidase studied by site-directed mutagenesis and resonance Raman spectroscopy, *Biochemistry 27*, 5477−5485.
55. Smulevich, G., Hu, S., Rodgers, K. R., Goodin, D. B., Smith, K. M., and Spiro, T. G. (1996) Heme-protein interactions in cytochrome *c* peroxidase revealed by site-directed mutagenesis and resonance Raman spectra of isotopically labeled hemes, *Biospectroscopy 2*, 365−376.
56. Smulevich, G., Paoli, M., Burke, J. F., Smith, A. T., Sanders, S. A., and Thorneley, R. N. F. (1994) Characterization of Recombinant Horseradish Peroxidase C and three Site-Directed mutants, F41V, F41W, and R38K, by Resonance Raman Spectroscopy, *Biochemistry 33*, 7398−7407.
57. Hillar, A., Peters, B., Pauls, R., Loboda, A., Zhang, H., Mauk, A. G., and Loewen, P. C. (2000) Modulation of the activities of catalase-peroxidase HPI of *Escherichia coli* by site-directed mutagenesis, *Biochemistry 39*, 5868−5875.
58. Uno, T., Nishimura, Y., Tsuboi, M., Makino, R., Iizuka, T., and Ishimura, Y. (1987) Two types of conformers with distinct Fe−C−O configuration in the ferrous CO complex of horseradish peroxidase. Resonance Raman and infrared spectroscopic studies with native and deuterioheme-substituted enzymes, *J. Biol. Chem. 262*, 4549−4556.
59. Rodriquez-Lopez, J. N., George, S. J., and Thorneley, R. N. F. (1998) The structure of carbonyl horseradish peroxidase: spectroscopic and kinetic characterization of the carbon monoxide complexes of His-42 → Leu and Arg-38 → Leu mutants, *J. Biol. Inorg. Chem. 3*, 44−52.
60. Edwards, S. L., and Poulos, T. L. (1990) Ligand binding and structural perturbations in cytochrome *c* peroxidase. A crystallographic study, *J. Biol. Chem. 265* (5), 2588−2595.
61. Gajhede, M., Schuller, D. J., Henriksen, A., Smith, A. T., and Poulos, T. L. (1997) Crystal structure of horseradish peroxidase C at 2.15 Å resolution, *Nat. Struct. Biol. 4*, 1032−1038.
62. Yu, N.-T., Kerr, E. A., Ward, B., and Chang, C. K. (1983) Resonance Raman detection of Fe−CO stretching and Fe−C−O bending vibrations in sterically hindered carbonmonoxy "strapped hemes". A structural probe of Fe−C−O distortion, *Biochemistry 22*, 4534−4540.
63. Hu, S., Treat, R., and Kincaid, J. R. (1993) Distinct Heme-Active Site Structure in Lactoperoxidase Revealed by Resonance Raman Spectroscopy, *Biochemistry 32*, 10125−10130.
64. Li, X. Y., and Spiro, T. G. (1988) Is bound carbonyl linear or bent in heme proteins? Evidence from resonance Raman and infrared spectroscopic data, *J. Am. Chem. Soc. 110*, 6024−6033.
65. Ray, G. B., Li, X. Y., Ibers, J. A., Sessler, J. L. and Spiro, T. G. (1994) How far can proteins bend the FeCO unit? Distal polar and steric effects in heme proteins and models, *J. Am. Chem. Soc. 116*, 162−176.
66. Enemark, J. H., and Feltham, R. D. (1974) Principles of structure, bonding, and reactivity for metal nitrosyl complexes, *Coord. Chem. Rev. 13*, 339−406.
67. Hu, S., and Kincaid, J. R. (1991) Resonance Raman spectra of the nitric oxide adducts of ferrous cytochrome P450cam in the presence of various substrates, *J. Am. Chem. Soc. 113*, 9760−9766.
68. Yu, N.-T., Lin, S. H., Chang, C. K., and Gersonde, K. (1989) Resonance Raman enhancement of the manganese−nitrogen−oxygen bending mode in nitrosyl manganese "strapped" and "open" heme complexes, *Biophys. J. 55*, 1137−1144.
69. Hu, S., and Kincaid, J. R. (1993) Heme active-site structural characterization of chloroperoxidase by resonance Raman spectroscopy, *J. Biol. Chem. 268*, 6189−6193.
70. Maes, E. M., Walker, F. A., Montfort, W. R., and Czernuszewicz, R. S. (2001) Resonance Raman Spectroscopic Study of Nitrophorin 1, a Nitric Oxide-Binding Heme Protein from Rhodnius prolixus, and Its Nitrosyl and Cyano Adducts, *J. Am. Chem. Soc. 123*, 11664−11672.
71. Hu, S., and Kincaid, J. R (1991) Resonance Raman characterization of nitric oxide adducts of cytochrome P450cam: The effect of substrate structure on the iron-ligand vibrations, *J. Am. Chem. Soc. 113*, 2843−2850.
72. Wengenack, N. L., Todorovic, S., Yu, L., and Rusnak, F. (1998) Evidence for differential binding of isoniazid by *Mycobacterium tuberculosis* KatG and the isoniazid-resistant mutant KatG(S315T), *Biochemistry 37*, 15825−15834.
73. Ghiladi, R. A., Cabelli, D. E., and Ortiz de Montellano, P. R. (2004) Superoxide reactivity of KatG: Insights into isoniazid resistance pathways in TB, *J. Am. Chem. Soc. 126*, 4772−4773.
74. Wengenack, N. L., Hoard, H. M., and Rusnak, F. (1999) Isoniazid oxidation by *Mycobacterium tuberculosis* KatG: A role for superoxide which correlates with isoniazid susceptibility, *J. Am. Chem. Soc. 121*, 9748−9749.
75. Henriksen, A., Schuller, D. J., Meno, K., Welinder, K. G., Smith, A. T., and Gajhede, M. (1998) Structural Interactions between Horseradish Peroxidase C and the Substrate Benzhydroxamic Acid Determined by X-ray Crystallography, *Biochemistry 37*, 8054−8060.
76. Holzbaur, I. E., English, A. M., and Ismail, A. A. (1996) Infrared spectra of carbonyl horseradish peroxidase and its substrate complexes: Characterization of pH-dependent conformers, *J. Am. Chem. Soc. 118*, 3354−3359.
77. Chelikani, P., Carpena, X., Fita, I., and Loewen, P. C. (2003) An Electrical Potential in the Access Channel of Catalases Enhances Catalysis, *J. Biol. Chem. 278*, 31290−31296.
78. Nicholls, P., Fita, I., and Loewen, P. C. (2001) Enzymology and structure of catalases, *Adv. Inorg. Chem. 51*, 51−106.
79. Chottard, G., and Mansuy, D. (1977) Resonance Raman studies of hemoglobin complexes with nitric oxide, nitrosobenzene and nitrosomethane: observation of the metal−ligand vibrations, *Biochem. Biophys. Res. Commun. 77*, 1333−1338.
80. Sampath, V., Zhao, X. J., and Caughey, W. S. (1994) Characterization of interactions of nitric oxide with human hemoglobin A by infrared spectroscopy, *Biochem. Biophys. Res. Commun. 198*, 281−287.
81. Ding, X. D., Weichsel, A., Andersen, J. F., Shokhireva, T. K., Balfour, C., Pierik, A. J., Averill, B. A., Montfort, W. R., and Walker, F. A. (1999) Nitric Oxide Binding to the Ferri- and Ferroheme States of Nitrophorin 1, a Reversible NO−Binding Heme Protein from the Saliva of the Blood-Sucking Insect, *Rhodnius prolixus*, *J. Am. Chem. Soc. 121*, 128−138.
82. Pinakoulaki, E., Gemeinhardt, S., Saraste, M., and Varotsis, C. (2002) Nitric-oxide Reductase. Structure and properties of the catalytic site from Resonance Raman scattering, *J. Biol. Chem. 277*, 23407−23413.

BI048097F